High-Resolution Crystal Structures of Human Hemoglobin with Mutations at Tryptophan 37β: Structural Basis for a High-Affinity T-State[†,‡]

Jeffrey S. Kavanaugh, Jamie A. Weydert, Paul H. Rogers, and Arthur Arnone*

Department of Biochemistry, College of Medicine, The University of Iowa, Iowa City, Iowa 52242

Received April 15, 1997; Revised Manuscript Received November 20, 1997

ABSTRACT: The high-resolution X-ray structures of the deoxy forms of four recombinant hemoglobins in which Trp37(C3)β is replaced with Tyr (βW37Y), Ala (βW37A), Glu (βW37E), or Gly (βW37G) have been refined and analyzed with superposition methods that partition mutation-induced perturbations into quaternary structure changes and tertiary structure changes. In addition, a new cross-validation statistic that is sensitive to local changes in structure (a "local R_{free}" parameter) was used as an objective measure of the significance of the tertiary structure changes. No significant mutation-induced changes in tertiary structure are detected at the mutation site itself for any of the four mutants studied. Instead, disruption of the intersubunit contacts associated with Trp37(C3)β results in (1) a change in quaternary structure at the $\alpha1\beta2$ interface, (2) α subunit tertiary structure changes that are centered at Asp94(G1)α−Pro95(G2)α, (3) β subunit tertiary structure changes that are located between residues Asp99(G1)β and Asn102(G4)β, (4) increased mobility of the α subunit COOH-terminal dipeptide, and (5) shortening of the Fe−N$^{\epsilon2}$His(F8) bond in the α and β subunits of the βW37G and βW37E mutants. In each case, the magnitude of the change in a particular structural parameter increases in the order βW37Y < βW37A < βW37E ≈ βW37G, which corresponds closely to the degree of functional disruption documented in the preceding papers.

Determining the stereochemical basis for the low oxygen affinity of the deoxyhemoglobin $\alpha_2\beta_2$ tetramer is central to a full understanding of the cooperative mechanism of hemoglobin action. The intrinsic oxygen affinity of the deoxyhemoglobin tetramer is nearly 300-fold lower than the oxygen affinity of free $\alpha\beta$ dimers (*1*), indicating that atomic interactions unique to the subunit−subunit interfaces of the tetramer oppose ligation-induced structural transitions. In particular, detailed crystallographic studies have identified the dynamic $\alpha1\beta2$ interface as the likely location for structural constraints that control hemoglobin oxygen affinity (*2*−*4*), and thermodynamic analysis of the cooperative free energies of mutant and chemically modified hemoglobins (*5*) has found strong energetic coupling between cooperativity and the noncovalent interactions at $\alpha1\beta2$ interface.

The $\alpha1\beta2$ interface is composed of a large number of noncovalent interactions, some of which can be disrupted or eliminated without greatly altering the functional properties of hemoglobin (*5*). In particular, recent crystallographic and solution studies of mutations at Tyr35(C1)β, a residue that is spatially adjacent to Trp37(C3)β, only detected very minor changes in the structures and functional properties of the mutants βY35F and βY35A (Kavanaugh et al., in preparation). In other cases, the loss of relatively few $\alpha1\beta2$ interactions has more significant consequences (*5*, *6*), with mutations of Trp37(C3)β being among the most disruptive. Previous studies (*7*−*12*) have shown that mutations at Trp37(C3)β severely destabilize the $\alpha1\beta2$ interface, and the altered functional properties of these mutants have been attributed largely to the formation of $\alpha\beta$ dimers. However, the accompanying papers (*13*−*15*) show that a large shift in the tetramer-to-dimer equilibrium is not sufficient to account for the wide range of altered functional properties of the mutants βW37Y,[1] βW37A, βW37E, and βW37G. In particular, the βW37E and βW37G *tetramers* are perturbed to such an extent that their functional properties are similar to those of $\alpha\beta$ dimers—having very high oxygen affinities with no cooperativity (*13*) and extremely fast CO combination rates (*14*). This implies that in these two 37β mutants the structural constraints at the $\alpha1\beta2$ interface of the deoxyhemoglobin tetramer are almost completely eliminated. Moreover, the constraints are only minimally restored by chemi-

[†] This work was supported by National Institutes of Health Program Project Grant PO1 HL51084. J.S.K. was supported by NIH Institutional Training Grants T32-HL07121 and T32-HL07344.

[‡] Refined coordinates and structure factors have been deposited in the Brookhaven Protein Data Bank. The accession numbers for the βV1M, βW37Y, βW37A, βW37G, and βW37E coordinates in crystal form 1 are 1A0U, 1A0V, 1A0W, 1AAA0X, and 1A0Y, respectively. The corresponding accession numbers for crystal form 1 structure factors are R1A0USF, R1A0VSF, R1A0WSF, R1A0XSF, and R1A0YSF, respectively. The accession numbers for the βV1M and βW37Y in crystal form 2 are 1A0Z and 1A00 for coordinates and R1A0ZSF and R1A00SF for structure factors. The accession numbers for βW37A in crystal form 3 are 1A01 for coordinates and R1A01SF for structure factors.

[1] Abbreviations: PEG, poly(ethylene glycol); rms, root mean square; βV1M, recombinant hemoglobin with the Val 1β → Met mutation; βW37Y, recombinant hemoglobin with the Trp 37β → Tyr and Val 1β → Met mutations; βW37A, recombinant hemoglobin with the Trp 37β → Ala and Val 1β → Met mutations; βW37G, recombinant hemoglobin with the Trp 37β → Gly and Val 1β → Met mutations; βW37E, recombinant hemoglobin with the Trp 37β → Glu and Val 1β → Met mutations; R value = $\Sigma||F_o| - |F_c||/\Sigma|F_o|$; $R_{sym} = \Sigma_{hkl}[|(I_{hkl} - I_{hkl}|]/\Sigma_{hkl}(\overline{I_{hkl}})$.

S0006-2960(97)00870-2 CCC: $15.00
Published on Web 03/17/1998

cally cross-linking the two $\alpha\beta$ dimers together (*13*, *14*). On the other hand, the functional properties of the βW37Y and βW37A tetramers are altered to a much smaller degree, implying that in these mutants the constraints imposed by the $\alpha1\beta2$ interface are still partially intact.

To compare the relative magnitudes of the structural differences between mutants in a straightforward manner, the X-ray studies of the βW37Y, βW37A, βW37E, and βW37G tetramers were carried out in the same crystal lattice using the same computational protocols. This permitted the detection of very small mutation-induced changes in protein structure with magnitudes that increase in an order (βW37Y < βW37A < βW37E $\approx$ βW37G) that corresponds closely to the degree of functional disruption documented in the preceding papers. The absence of significant tertiary structure changes in the βW37Y mutant, and the very small tertiary structure changes in the βW37A mutant, were confirmed by repeating the structural analyses in a second crystal lattice. In addition, a new cross-validation statistic that is sensitive only to local changes in structure (a "local R_{free}" parameter) provided another objective measure of the significance of the tertiary structure changes.

MATERIALS AND METHODS

Mutant hemoglobins were made and purified by Kwiatkowski et al. (*14*). They were overexpressed in *Escherichia coli* using the T7 expression system developed by Hernan et al. (*16*). As described previously, the "wild-type" hemoglobin used in this study (βV1M) is a surrogate for hemoglobin A in which the β subunit NH_2-terminal valine is replaced by methionine (*16*−*18*). This valine-to-methionine substitution is necessitated by the differences in amino-terminal processing in mammals and bacteria. Therefore, all the 37β mutants also contain the βV1M substitution, and all structural comparisons are versus βV1M. It is important to note that previous studies documented in detail the lack of any significant structural or functional consequences of the βV1M mutation.

Crystal Growth. Prior to crystallization all mutant hemoglobins were stripped of organic and inorganic ions by passing them over a Dintzis column (*19*) that was modified by the addition of a 1 mm layer of chelating resin (iminodiacetic acid, Sigma No. C-7901) to the top of the column. The stripped oxyhemoglobins were frozen and stored in liquid nitrogen until they were used for crystallization. All crystallization solutions were thoroughly deoxygenated prior to use, and all crystallization work was conducted in a glovebag that was continuously purged with nitrogen.

Crystals of βV1M deoxyhemoglobin and isomorphous crystals of the deoxy forms of βW37Y, βW37A, βW37G, and βW37A (Table 1) were grown at room temperature using the batch method previously described (*20*, *21*) with the addition of a seeding step (*22*). Specifically, small seed crystals (approximately $0.05 \times 0.05 \times 0.01$ mm^3) of deoxyhemoglobin A were drifted through a small glass pipet that was filled with the buffered crystallization solution (10 mM potassium phosphate at pH 7.0, 100 mM potassium chloride, 3 mM sodium dithionite, and 10.0% PEG 6000) and then injected into 100 μL of the same crystallization solution (where the concentration of PEG 6000 ranged between 10.0% and 10.5%) that also contained 10 mg/mL hemoglobin. The seeds grew into well-formed crystals within 2−3 weeks.

Table 1

hemoglobin	crystal form	space group	unit cell constants[a] *a* (Å)	*b* (Å)	c (Å)	β (deg)
βV1M	1	$P2_12_12$	97.2	99.3	65.9	
βW37Y	1	$P2_12_12$	97.2	99.4	66.1	
βW37A	1	$P2_12_12$	96.8	99.2	66.2	
βW37G	1	$P2_12_12$	96.4	99.3	66.3	
βW37E	1	$P2_12_12$	96.7	99.1	66.3	
βV1M	2	$P2_12_12_1$	83.9	112.0	63.7	
βW37Y	2	$P2_12_12_1$	84.1	112.0	63.8	
βV1M	3	$P2_1$	63.2	83.7	53.8	99.4
βW37A	3	$P2_1$	63.4	83.6	53.8	99.3

[a] The uncertainty in these measurements is about 0.1 Å and 0.1°.

In the absence of the seeding procedure, recombinant hemoglobins with the βV1M substitution occasionally crystallize from the same PEG solutions in a different orthorhombic crystal form that was first reported for Hb M Iwate (*23*) and subsequently for Hb C (*24*). More recently, this crystal form has been obtained with stripped deoxyhemoglobin A crystallized from solutions of 12%−14% PEG 1450 (Chan and Arnone, unpublished results). The structures of deoxy-βV1M and deoxy-βW37Y in this crystal form are reported below (see crystal form 2 in Table 1).

"High-salt" crystals (crystal form 3 in Table 1) of the deoxy βW37A mutant hemoglobin were grown in 100 μL batch setups at room temperature from solutions of concentrated ammonium sulfate as described by Perutz (*25*) for deoxyhemoglobin A. The βW37A crystals are isomorphous with high-salt βV1M crystals (Table 1).

Diffraction Data Collection. Following a brief washing in a substitute mother liquor that contained 13% PEG 6000 and 3 mM sodium dithionite, single crystals of the mutant deoxyhemoglobins and deoxy βV1M in crystal forms 1 and 2 were mounted in quartz capillaries for data collection. A single crystal of deoxy-βW37A in crystal form 3 was washed briefly in the high salt crystallization buffer in which the total salt concentration was increased to 2.6 M and mounted in a quartz capillary. Diffraction data were collected on a Rigaku AFC6 diffractometer fitted with a San Diego Multiwire Systems area detector. All diffraction data were scaled and merged according to the procedure of Howard et al. (*26*). In each case, degradation due to radiation damage was less than 15% as determined from a subset of diffraction data that was collected at the beginning and end of data collection. The statistics presented in Table 2 show that in crystal form 1 diffraction data of comparable resolution were collected for βW37A, βW37G, and βW37E and that slightly lower resolution diffraction data were collected for βW37Y and βV1M. Higher resolution (2.0 Å) diffraction data were collected for βW37Y and βV1M in crystal form 2. A 1.8 Å diffraction data set (Table 2) was collected for deoxy-βW37A in crystal form 3. The βW37A data set is of comparable resolution to the data set used to refine the structure of βV1M in the high-salt crystal form 3 (*18*). The diffraction data sets for each 37β mutant (Table 2) were split into a working data set (consisting of 90% of the data) that was used for refinement and a cross-validation data set (consisting of the remaining 10% of the data) that was used to calculate the Brünger R_{free} value (*27*).

Table 2: Summary of X-ray Diffraction Data

hemoglobin	crystal form	total observations	unique reflections	resolution (Å)	% complete	(%) R_{sym}[a]	reflections in working set ($I > 2\sigma$)	reflections in R_{free} set ($I > 2\sigma$)
βV1M	1	267 646	35 230	2.14	98.1	7.9	33 920	
βW37Y	1	234 062	31 603	2.22	97.9	11.1	26 982	2684
βW37A	1	265 817	42 934	1.99	97.1	6.5	36 531	3625
βW37G	1	268 927	44 737	1.93	91.7	8.6	37 418	3743
βW37E	1	267 181	43 340	1.98	96.7	7.9	36 174	3619
βV1M	2	262 565	40 065	2.00	96.8	8.8	39 110	
βW37Y	2	237 463	40 226	2.00	97.1	6.9	34 844	3470
βW37A	3	460 141	49 388	1.80	96.3	3.6	44 030	4411

[a] $R_{sym} = \Sigma_{hkl}[|\overline{I_{hkl}} - I_{hkl}|]/\Sigma_{hkl}\overline{I_{hkl}}$.

Table 3: Refinement Summary

	hemoglobin/crystal form																	
	βW37Y/1			βW37A/1			βW37E/1			βW37G/1			βW37Y/2			βW37A/3		
refinement step	R	R_{free}	no. of cycles	R	R_{free}	no. of cycles	R	R_{free}	no. of cycles	R	R_{free}	no. of cycles	R	R_{free}	no. of cycles	R	R_{free}	no. of cycles
initial model	0.224	0.214		0.252	0.249		0.293	0.295		0.330	0.328		0.243	0.239		0.207	0.206	
rigid-body tetramer	0.215	0.205	20	0.241	0.236	20	0.285	0.289	20	0.314	0.310	20	0.195	0.191	20	0.206	0.208	20
rigid-body dimer	0.209	0.202	20	0.225	0.222	20	0.253	0.259	20	0.270	0.272	20	0.191	0.187	20	0.205	0.206	20
rigid-body subunits	0.207	0.199	20	0.214	0.212	20	0.237	0.243	20	0.253	0.253	20	0.188	0.185	20	0.197	0.200	20
PROLSQ (37βAla)	0.184	0.235	16	0.175	0.244	32	0.194	0.250	16	0.191	0.259	64	0.167	0.223	16	0.169	0.223	16
final PROLSQ cycles	0.166	0.256	62				0.181	0.256	55				0.160	0.224	7			

Refinement of βV1M Structures in Crystal Forms 1 and 2. The starting model for the deoxy-βV1M refinement in crystal form 1 was constructed from the isomorphous 2.1 Å deoxyhemoglobin A model (*28*) by converting the NH_2-terminal valine residue of each β subunit into an alanine residue. The initial R value for this model (including solvent molecules) was 0.187 for all the diffraction data between 8.0 and 2.1 Å resolution with magnitudes greater than 2σ (33 920 reflections). The R value dropped to 0.180 after 11 cycles of stereochemically restrained least-squares refinement with the program PROLSQ (*29, 30*). The methionine side chains of the β NH_2 termini were then added to the atomic model, and the beginning portions of the β subunits were refit into $F_o - F_c$ omit maps using the computer graphics program TOM/FRODO (*31, 32*). After 10 additional cycles of least-squares refinement, the R value for the final deoxy-βV1M model in crystal form 1 was 0.176 for all diffraction data between 8.0 and 2.1 Å resolution with magnitudes greater than 2σ. Except for small changes in structure at the β NH_2 termini, the crystal structure of βV1M is virtually identical with the corresponding structure of deoxyhemoglobin A.

The initial model for the deoxy-βV1M refinement in crystal form 2 was constructed from the isomorphous 1.8 Å deoxyhemoglobin A model (Chan and Arnone, unpublished results) by converting the NH_2-terminal valine residue of each β subunit into an alanine residue. The initial R value for this model (including solvent molecules) was 0.191 for all the diffraction data between 8.0 and 2.0 Å resolution with magnitudes greater than 2σ (39 110 reflections). The R value dropped to 0.164 after 25 cycles of stereochemically restrained least-squares refinement with the program PROLSQ. The full methionine side chains of the β NH_2 termini were then added to the atomic model, and the beginning portions of the β subunits were refit into $F_o - F_c$ omit maps. The remainder of refinement consisted of 25 least-squares refinement cycles and a second round of visual refitting of the β subunit NH_2 termini, followed by 8 refinement cycles. The R value for the final deoxy-βV1M model in crystal form 2 was 0.167. The differences between the structures of βV1M and deoxyhemoglobin A in crystal form 2 are small and are confined to the NH_2-terminal regions of the β subunits.

Refinement of 37β Mutant Structures in Crystal Forms 1, 2, and 3. Each recombinant 37β mutant structure was refined using the same procedures, namely rigid-body refinement using the program X-PLOR (*33*) followed by stereochemically restrained least-squares refinement with the program PROLSQ. The same working and test data sets were used for the rigid-body and least-squares refinements. In each case the mutant atomic models were refined against the diffraction data between 8.0 Å and the upper resolution limit (2.2−1.8 Å depending on the mutation) with structure factors of magnitude 2σ or greater (Table 2). The starting model for the refinement of each mutant structure was the deoxy-βV1M structure in the appropriate crystal lattice with alanine (or glycine in the case of βW37G) at residue 37β. The course of each refinement is summarized in Table 3. In each case, stereochemically restrained least-squares refinement was carried out until no further tertiary structures changes were detected with δ_3 plots (see below).

All of the atomic models have comparable stereochemistry with rms deviations from ideal bond lengths that range from 0.010 to 0.013 Å and rms deviations from ideal bond angles of 1.6° or less. Analysis with PROCHECK (*34*) indicates

that at least 91% of all residues in each structure are located within the "most favored" regions of a Ramachandran plot and the remainder of the residues are found in the "additional allowed" regions. No residues are located within the "generously allowed" or disallowed regions of the plot. All the other parameters calculated by PROCHECK are within the expected range of values or better than expected for the resolution of a given data set.

Analysis Fe−N$^{\epsilon 2}$His(F8) Bond Lengths. A systematic approach was used to determine if the mutation-induced structural perturbations included changes in the lengths of the α or β subunit Fe−N$^{\epsilon 2}$His(F8) covalent bonds in crystal form 1. Specifically, the PROLSQ target value for the Fe−N$^{\epsilon 2}$His(F8) bond length was varied over a range of target values about the normally accepted "ideal" value of ∼2.2 Å (*35*). Fifteen least-squares refinement cycles were run for each target distance. The residuals between the refined Fe−N$^{\epsilon 2}$ distances and the target values for these distances were plotted versus target value in order to obtain the Fe−N$^{\epsilon 2}$ distance that resulted in a residual of zero, the "zero residual" Fe−N$^{\epsilon 2}$ distance, for each of the 37β mutants. The 37β refinements in crystal form 1 were completed by running 30 more cycles of least-squares refinement using these zero residual Fe−N$^{\epsilon 2}$ distances as target values. The average Fe−N$^{\epsilon 2}$His(F8) bond lengths in the final 37β atomic models agree very well (within 0.002 Å) with the Fe−N$^{\epsilon 2}$His(F8) target lengths. These refinement cycles did not have a significant effect on the *R* values, R_{free} values, or the stereochemistry of the atomic models.

Structure Analysis. Superpositions of the atomic models were carried out using the method of Kabsch (*36*) as implemented in the program BMFIT (*37*). An iterative superposition procedure similar to the "sieve fit" procedure of Gerstein and Chothia (*38*) was used to define a "static core" of main chain atoms for each subunit of the 37β mutant hemoglobins. Specifically, individual subunits of the mutant atomic models were superimposed onto the corresponding βV1M subunits, and residues with atomic displacements greater than twice the rms displacement value were omitted from subsequent superpositions. Typically this procedure converged within three to five superposition cycles. The static cores of the mutant hemoglobin subunits ranged in size from 312 to 484 main chain atoms, and the rms residuals ranged from 0.08 to 0.14 Å.

To identify the location of mutation-induced tertiary structure changes, the magnitude of the main chain displacement vector, $\vec{\delta}_3$, was plotted versus residue number. In general, $|\vec{\delta}_n|$ is defined as

$$|\vec{\delta}_n| = \delta_n = \frac{1}{4n}\left|\sum_{j=1}^{4n}\Delta\vec{r}_j\right|$$

where the summation is carried out over n contiguous residues and $\Delta\vec{r}_j$ is the atomic displacement vector for the *j*th main chain atom of the n-residue peptide. Concerted structural changes result in the constructive addition of the $\Delta\vec{r}_j$ vectors, whereas poorly correlated structural differences will tend to diminish the magnitude of $\vec{\delta}_n$. (In contrast, a simple rms difference between two different structures does not distinguish between correlated and uncorrelated differences.) As *n* increases from 1 to 5, the magnitude of the peaks in the δ_n plots decreases while the signal-to-noise ratio tends to reach to maximum value at about 3 for the 37β mutants. Therefore, δ_3 plots are used to analyze the movements of entire peptide segments, while δ_1 values are used to specifically describe the mutation-induced shifts of individual residues.

The change in quaternary structure for each mutant was characterized as a rigid body screw rotation (*3, 39*). Specifically, each atomic model was first transformed to a standard orientation in which the dyad axis of the $\alpha_2\beta_2$ tetramer was positioned along the *y*-axis, and the *x*-axis was aligned along the line defined by the α1Fe−β1Fe and α2Fe−β2Fe midpoints. Once in the standard orientation, the backbone atoms of the α1β1 and α2β2 dimers were averaged, yielding a tetramer with exact 2-fold symmetry. Next the α1β1 dimer of a given 37β mutant was superimposed on the βV1M α1β1 dimer using the sieve fit protocol described above. Then the α2β2 dimer of βV1M was superimposed on the α2β2 dimer of the repositioned 37β mutant tetramer. The screw rotation parameters associated with this last transformation define the mutation-induced quaternary structure change.

Accessible surface areas were calculated for the βV1M and 37β mutant tetramers using the Lee and Richards algorithm (*40*) as implemented in X-PLOR (*33*). The default water molecule radius of 1.6 Å and default accuracy setting of 0.05 were used during the calculations. The buried surface area of residue 37β was calculated as the difference between its accessible surface in an αβ dimer and its accessible surface in the $\alpha_2\beta_2$ tetramer.

Cross-Validation of Tertiary Structure Changes Using a Local R_{free} Parameter. The validity of the small, mutation-induced tertiary structure changes was assessed with a variant of the Brünger R_{free} parameter (*27*) that is calculated as follows. After convergence of the PROLSQ refinement of a particular mutant hemoglobin, "hybrid" atomic models were generated by replacing every three-residue peptide in both α chains or both β chains of the starting PROLSQ model with the corresponding peptides from the fully refined atomic model.[2] Thus 283 hybrid atomic models were generated (139 α chain models and 144 β chain models), and each of these hybrid models was used to calculate a corresponding R_{free} value, the R_{free}^{local} value. Since the replacement of 6 out of 574 residues represents only about 1% of the refined model, large variations in R_{free}^{local} cannot occur. However, if the structural changes associated with a particular tripeptide represent an improvement to the starting model, the R_{free}^{local} value calculated with the hybrid model containing this tripeptide should be reduced slightly relative to the R_{free} value calculated with the unaltered starting model. Therefore, the R_{free}^{local} value is a statistic that is sensitive only to structural changes in a particular tripeptide.

RESULTS

Least-squares superposition methods and δ_3 plots (see Materials and Methods and *28*) were used to partition the structural changes that result from the 37β mutations into

[2] The tripeptide window size was chosen because the smallest mutation-induced tertiary structure changes detected by superposition analysis (see above and Results) extend over approximately three contiguous residues.

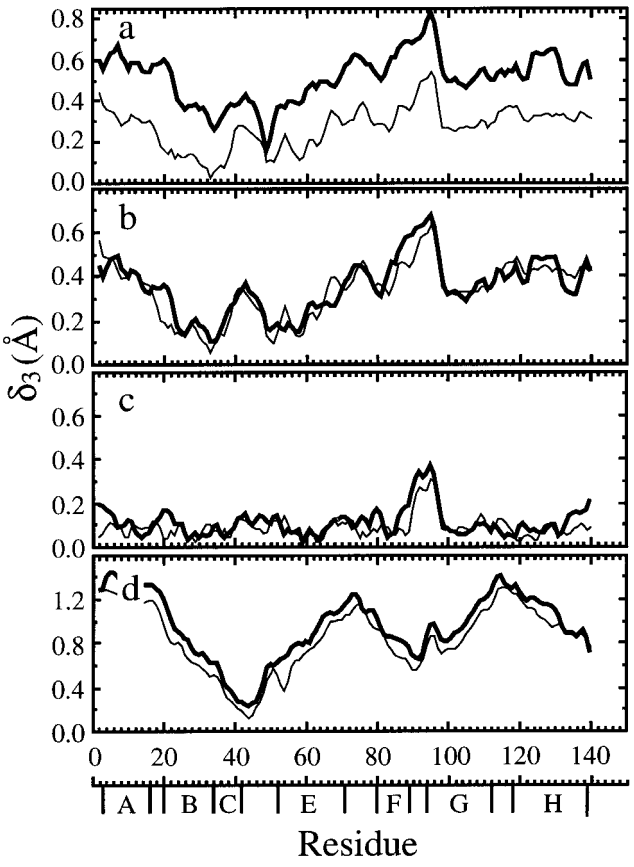

FIGURE 1: δ_3 plots for the main chain atoms of the α1 (thin lines) and α2 (thick lines) subunits of βW37E in crystal form 1. (a) δ_3 was calculated before any superposition of the βW37E and βV1M deoxyhemoglobin coordinates. (b) δ_3 was calculated after "sieve fit" superposition (see text) of the βW37E and βV1M tetramers. (c) δ_3 was calculated after "sieve fit" superposition of the individual α subunits of βW37E and βV1M. (d) δ_3 was calculated after "sieve fit" superposition of the individual β subunits (on the opposite $\alpha\beta$ dimer) of βW37E and βV1M. The boundaries of helices A through H are indicated on the axis located at the bottom of the figure.

components of (1) a rigid-body movement of the tetramer, (2) a change in quaternary structure, and (3) changes in tertiary structure. The δ_3 plots shown in Figure 1 illustrate this type of analysis for the α subunits of the βW37E mutant in crystal form 1. The different δ_3 magnitudes of the α1 subunit and α2 subunit δ_3 profiles in the absence of any superposition (Figure 1a) indicate that the Trp → Glu mutation has altered the position of the entire tetramer within the crystal lattice. Superimposing the βV1M (the wild-type structure) and βW37E tetramers before calculating a δ_3 plot removes the mutation-induced rigid-body motion of the tetramer. The resulting δ_3 plot (Figure 1b) reflects the composite changes in quaternary structure and α subunit tertiary structure. The changes in tertiary structure can be isolated from the quaternary structure change by superimposing individual subunits of the βW37E atomic model on the corresponding subunits of the βV1M model and then calculating δ_3 plots for the superimposed subunits. When this is done, the δ_3 plot in Figure 1c (referred to below as a tertiary δ_3 profile) shows that the mutation-induced changes in the tertiary structure of the α subunits occur at the end of the F helix, the entire FG corner, and the beginning of the G helix, with the maximum perturbation occurring at Pro95-(G2)α. Figure 1d, on the other hand, illustrates a graphical

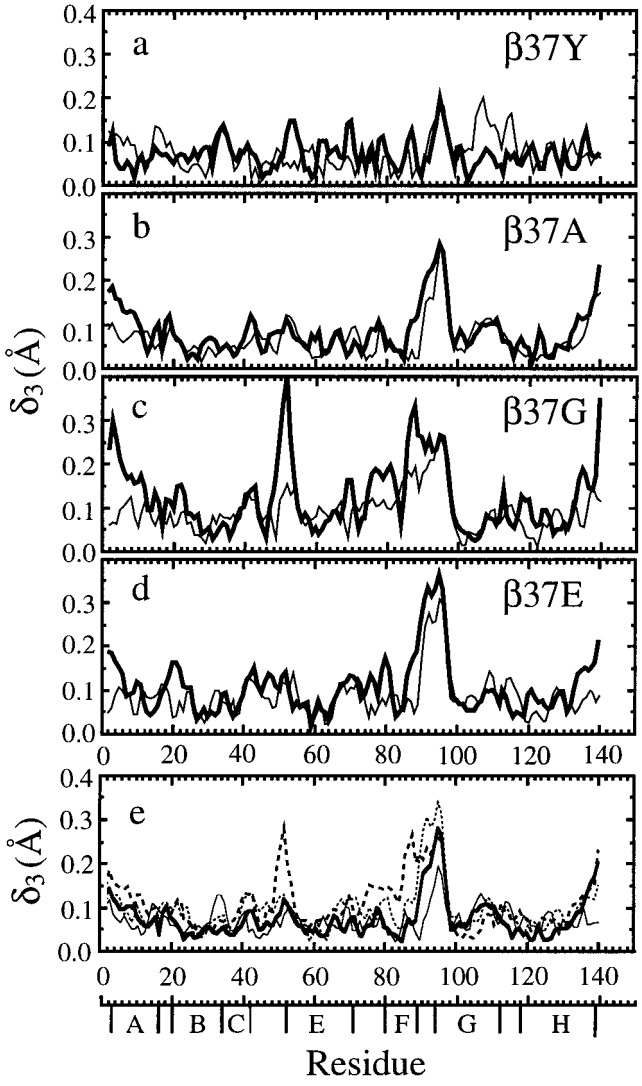

FIGURE 2: Tertiary δ_3 plots (calculated as in Figure 1c) for the main chain atoms of the α1 subunits (thin lines) and α2 subunits (thick lines) of βW37Y (a), βW37A (b), βW37G (c), and βW37E (d) in crystal form 1. The average of the α1 subunit and α2 subunit δ_3 plots for the main chain atoms are shown (e) for βW37Y (thin solid line), βW37A (thick solid line), βW37G (thick dashed line), and βW37E (thin dashed line).

means of displaying the mutation-induced change in quaternary structure that occurs across the $\alpha1\beta2$ (or symmetry-related $\alpha2\beta1$) interface. It is obtained by superimposing the $\beta2$ (or $\beta1$) subunit of the βW37E atomic model on the $\beta2$ (or $\beta1$) subunit of the βV1M model and then calculating a δ_3 plot between the nonsuperimposed α1 (or α2) subunits. This type of plot is referred as a quaternary δ_3 profile, and when the quaternary structure is not altered by a mutation, it should be flat (see below).

Changes in Tertiary Structure. δ_3 plots illustrating the tertiary component of the mutation-induced structural changes for each of the 37β mutants in crystal form 1 are shown in Figure 2 for the α subunits and in Figure 3 for the β subunits. Sizable movements are detected for each mutant at the β subunit NH_2 termini, and to a lesser extent at the α subunit NH_2 termini, but these are probably not energetically significant because the first few residues of each subunit have very high temperature factors. Moreover, direct analysis of the X-ray diffraction data with the R_{free}^{local} parameter clearly

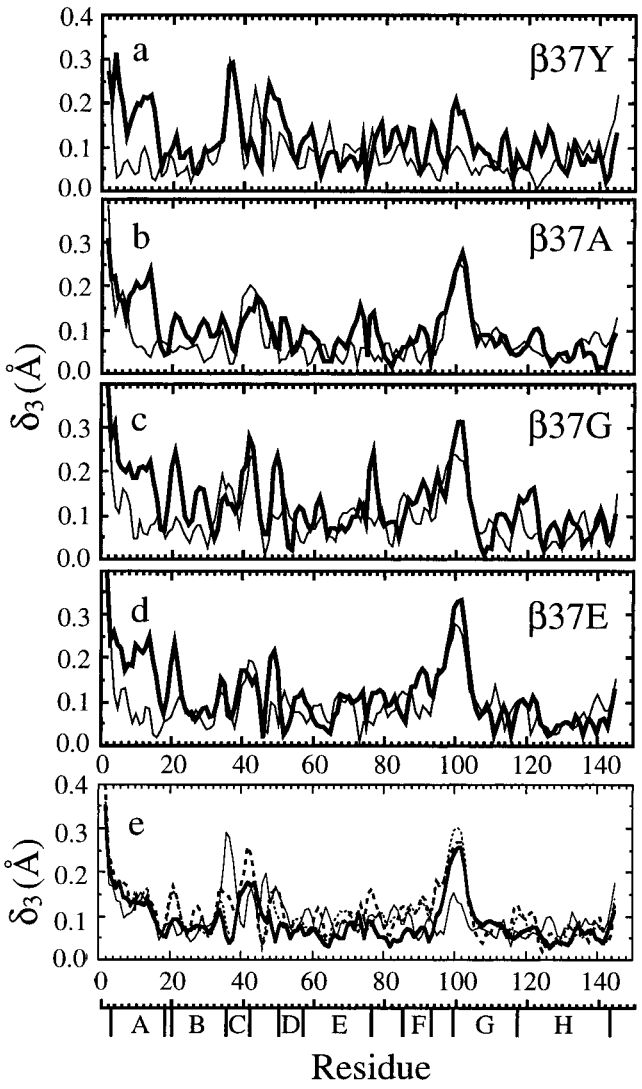

FIGURE 3: Tertiary δ_3 plots (calculated as in Figure 1c) for the main chain atoms of the β1 subunits (thin lines) and β2 subunits (thick lines) of βW37Y (a), βW37A (b), βW37G (c), and βW37E (d) in crystal form 1. The average of the β1 subunit and β2 subunit δ_3 plots for the main chain atoms are shown (e) for βW37Y (thin solid line), βW37A (thick solid line), βW37G (thick dashed line), and βW37E (thin dashed line).

indicates that these shifts do not improve the atomic model (see below). From Figures 2a and 3a it appears that the βW37Y mutation does not produce significant tertiary structure changes in either the α or the β subunits. In contrast, the βW37A mutation clearly results in perturbations to residues Leu91(FG3)α through Asn97(G4)α, which have δ_3 values between 0.17 and 0.28 Å with the maximum δ_3 value of 0.28 Å occurring at residue Pro95(G2)α. The only other significant change in the α subunit tertiary structure of βW37A occurs at the COOH termini. Similar α subunit structural changes were first observed when the deoxy form of the naturally occurring mutant βW37R (hemoglobin Rothschild) was compared to deoxyhemoglobin A (*28*). Figure 3b gives no indication of β subunit structural changes in the vicinity of the βW37A mutation site but does contain a peak between residues Asp99(G1)β and Asn102(G4)β which has δ_3 values between 0.22 and 0.26 Å. Similarly, the βW37G and βW37E mutations induce significant perturbations to the α subunit COOH termini and residues Leu91(FG3)α through Asn97(G4)α (Figure 2c,d), as well as the region between residues Asp99(G1)β and Asn102(G4)β (Figures 3c,d). In the α2 subunit of the βW37G mutant another δ_3 peak occurs at residues His50(CD8)α−Ser52(E1)α (Figure 2c). Since this peak is not observed in the α1 subunit, and since these residues are part of the mobile CD corner (with backbone temperature factors averaging about 40 Å^2), it may not be significant and as discussed below is not validated by the R_{free}^{local} parameter.

Even though the structural changes discussed above are small, most of them occur in both the α1β1 and α2β2 dimers. This implies that they are mutation-induced and therefore not due to random changes that can occur during the refinement process. Moreover, by averaging the α1/α2 and β1/β2 δ_3 profiles, the signal-to-noise ratio of the δ_3 plots can be significantly increased. The averaged α subunit and β subunit tertiary δ_3 profiles for all four mutants are overlaid in Figures 2e and 3e, respectively. In the case of the β subunits, the composite plot more clearly shows the δ_3 peak between residues Asp99(G1)β and Asn102(G4)β of the βW37A, βW37G, and βW37E mutants (with maximum values of 0.26 Å at 102 β, 0.27 Å at 101β, and 0.30 Å at 101β, respectively). In the case of the α subunits, the average δ_3 value at Pro95(G1)α is similar for βW37A, βW37G, and βW37E (with values of 0.28, 0.26, and 0.34 Å, respectively). The δ_3 peak for the βW37G mutant is much broader, with values greater than 0.2 Å extending from Leu86(F7)α through Val96(G3)α. In the averaged βW37Y δ_3 profiles, very small peaks occur at Pro95(G1)α ($\delta = 0.20$ Å) and Pro100(G1)β ($\delta = 0.15$ Å). Alone these βW37Y δ_3 peaks would not be considered significant. However, in the context of the corresponding larger peaks for the other 37β mutants they may represent genuine mutation-induced structural changes.

One way to assess the significance of these very small changes in tertiary structure is to determine whether they are reproducible in the context of a different crystal lattice. In Figure 4 tertiary δ_3 profiles are shown for the α subunits of βW37Y in crystal form 2 and for the α and β subunits of βW37A in crystal form 3. Again it is observed that if the βW37Y mutation perturbs the FG corner of the α subunit, the perturbation is very small (Figure 4a). The tertiary structure changes induced by the βW37A mutation to the α subunit FG corner and COOH terminus in crystal form 1 (Figure 2b) clearly are reproduced in crystal form 3 (Figure 4b). In the case of the β subunits of the βW37A mutant in crystal form 3 (Figure 4c), the δ_3 values for the NH_2 termini are very large, and there are two small δ_3 peaks: one centered at Glu101(G3)β and one at Leu78(EF7)β. The peak at Glu101(G3)β confirms the result found in crystal form 1. There is, however, no obvious counterpart in crystal form 1 for the small δ_3 peak at Leu78(EF7)β. Structure factor analysis using the R_{free}^{local} parameter (see below) validates the peaks at Pro95(G2)α and Glu101(G3)β but not the peak at the β EF corner or the changes at the NH_2 termini.

Changes in Quaternary Structure. In addition to altering the tertiary structure, each of the 37β mutations induces a quaternary structure change as shown by the relative heights of the averaged quaternary δ_3 profiles in Figure 5. Also included on this plot is an averaged quaternary δ_3 profile of deoxy-βV1M verses deoxyhemoglobin A in crystal from 1.

Table 4: Screw Rotation Analysis of Mutation-Induced Changes in Quaternary Structure

transition	crystal form	axis direction angles, α, β, γ (deg)	point on the axis, x, y, z (Å)	rotation angle (deg)	translation (Å)
Hb A → βV1M	1	47.3, 90.0, 42.7	0.0, 36.3, 0.0	0.1	0.0
βV1M → βW37Y	1	103.6, 90.0, 13.6	0.0, 14.4, 0.0	0.6	0.0
βV1M → βW37A	1	101.9, 90.0, 11.9	0.0, 16.6, 0.0	1.0	−0.1
βV1M → βW37E	1	105.1, 90.0, 15.1	0.0, 13.8, 0.0	1.6	−0.1
βV1M → βW37G	1	100.6, 90.0, 10.6	0.0, 11.6, 0.0	2.0	−0.1
Hb A → βW37R[a]	1	98.3, 90.0, 8.3	0.0, 8.8, 0.0	0.6	0.0
Hb A → βV1M	2	140.3, 90.0, 50.3	0.0, 16.4, 0.0	−0.1	0.0
βV1M → βW37Y	2	96.4, 90.0, 6.4	0.0, 33.1, 0.0	0.2	0.0
Hb A → βV1M[b]	3	41.7, 90.0, 48.3	0.0, 14.5, 0.0	0.1	0.0
βV1M → βW37A[a]	3	112.9, 90.0, 22.9	0.0, 48.9, 0.0	0.1	0.1

[a] Calculated using the previously reported Hb A and Hb Rothschild structures (*28*). [b] Calculated using the previously reported Hb A and βV1M structures (*18*).

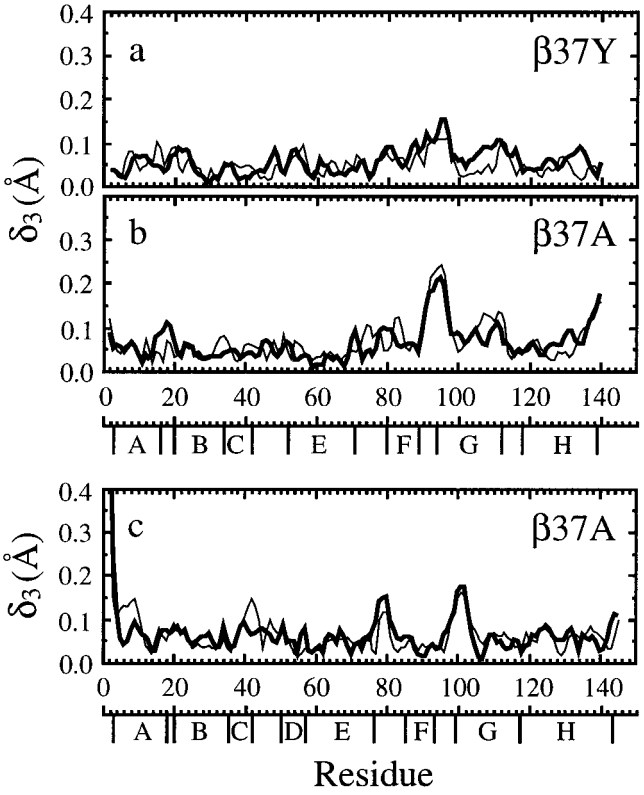

FIGURE 4: Tertiary δ_3 plots (calculated as in Figure 1c) for the main chain atoms of the α1 subunits (thin lines) and α2 subunits (thick lines) of βW37Y in crystal form 2 (a) and βW37A in crystal form 3 (b). (c) Tertiary δ_3 plots for the main chain atoms of the β1 subunits (thin lines) and β2 subunits (thick lines) of βW37A in crystal form 3.

The featureless βV1M δ_3 profile provides a measure of the sensitivity of this method in detecting mutation-induced changes in quaternary structure. Measured in this way, the magnitudes of the mutation-induced quaternary structure changes increase in the order βW37Y < βW37A < βW37E < βW37G.

The quaternary structure change for each mutant involves a rigid-body transformation of the $\alpha1\beta1$ dimer relative to the $\alpha2\beta2$ dimer that can be described as a screw rotation about a unique axis (*3*, *39*). Specifically, the $\alpha1\beta1$ dimer of each 37β mutant was superimposed onto the $\alpha1\beta1$ dimer of βV1M in a standard coordinate system that has the molecular dyad oriented along the *y*-axis (see Materials and Methods). The $\alpha2\beta2$ dimer of the βV1M atomic model was then superimposed onto the $\alpha2\beta2$ dimer of the repositioned 37β mutant atomic model. The screw rotation parameters that characterize the second superposition define the mutation-induced quaternary structure change (Table 4). From this analysis, it is clear that in crystal form 1 the quaternary structure transitions for all four 37β mutants have approximately the same screw rotation axis. This axis is perpendicular to and intersects the *y*-axis 11−17 Å below the origin, and it passes near the β subunit COOH-termini and below the "switch" region of the $\alpha1\beta2$ interface. Therefore, the rotations of 0.6°, 1.0°, 1.6°, and 2.0° about this axis for βW37Y, βW37A, βW37E, and βW37G, respectively, have the effect of progressively opening the "hinge" region of the $\alpha1\beta2$ interface.

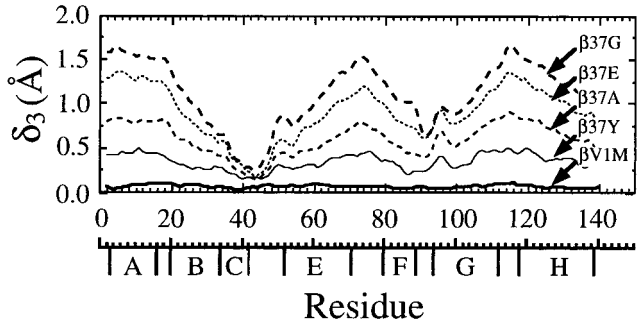

FIGURE 5: Quaternary δ_3 plot (calculated as in Figure 1d) showing the average of the α1 subunit and α2 subunit δ_3 plots for the main chain atoms of βW37Y, βW37A, βW37E, and βW37G in crystal form 1. Also included is a similar δ_3 profile that compares the βV1M atomic model with the deoxyhemoglobin A atomic model (*28*).

Very little evidence is found for a change in quaternary structure for the transitions HbA → βV1M crystal in forms 1, 2, or 3, βV1M → βW37Y in crystal form 2, and βV1M → βW37A in crystal form 3 (Table 4). In the case of the HbA → βV1M transition, the absence of a quaternary structure change in all three crystal forms is consistent with the results of Doyle et al. (*17*) that showed this mutation has almost no effect on the functional properties of hemoglobin. However, the lack of a quaternary structure change for the βV1M → βW37Y transition in crystal form 2 and the βV1M → βW37A transition in crystal form 3 is inconsistent with the observed quaternary structure changes for these same transitions in crystal form 1. This inconsistency is due mostly likely to differences in crystal packing. In particular, the crystal packing parameter V_M (*41*) varies from 2.46 Å^3/Da in crystal form 1 to 2.32 and 2.18 Å^3/Da in crystal forms 2 and 3, respectively. Thus crystal form 1 is the most loosely packed lattice, and therefore it is more likely to be able to accommodate large conformational changes. These differences in crystal packing are reflected

in the variation of the average temperature factor for the βV1M atomic models in crystal form 1 ($\langle B \rangle = 24.8$ Å^2), crystal form 2 ($\langle B \rangle = 20.7$ Å^2), and crystal form 3 ($\langle B \rangle = 19.7$ Å^2).

Mutation-Induced Structural Changes in the Hinge Region of the α1β2 Interface. The δ_3 profiles clearly reveal changes in both tertiary and quaternary structure that are centered in the hinge region of the α1β2 interface, the region of the 37β mutations. Figure 6a corresponds to the δ_3 plot in Figure 5 in that the atomic models of the β2 subunits of the 37β mutants have been superimposed on the β2 subunit of βV1M. Very little, if any, change in tertiary structure occurs at the 37β mutation site itself. In contrast, α1 subunit residues Leu91(FG3)α through Asn97(G4)α of all four mutants move away from the superimposed β2 subunits, and these movements are a composite of quaternary structure and α subunit tertiary structure changes. The magnitudes of these shifts increase in the order βW37Y < βW37A < βW37E ≅ βW37G, and this ordering of mutation-induced structural perturbations mirrors the relative increases in oxygen affinity and CO combination rates reported for these mutants in the accompanying papers (*13, 14*).

Figure 6b corresponds to the δ_3 plots in Figure 2 in that the atomic models of the α1 subunits of the 37β mutants have been superimposed on the α1 subunit of βV1M. The small movements of α1 subunit residues Leu91(FG3)α through Val96(G3)α are tertiary structure changes that result from the loss of α1β2 interface interactions, primarily the polar interaction between Asp94(G1)α1 and Trp37(C3)β2. In each case, the maximum tertiary structure change occurs at Pro95(G2)α1, where the δ_1 shifts of the main chain atoms are 0.22, 0.36, 0.34, and 0.42 Å for βW37Y, βW37A, βW37G, and βW37E, respectively. On the other hand, the shifts of β2 residues Tyr35(C1)β2 through Thr38(C4)β2 in Figure 6b reflect the *quaternary* structure changes that result from the loss of intersubunit interactions between residue 37β2 and several α1 subunit residues (see below).

In addition to these atomic displacements, the loss of intersubunit atomic interactions in the 37β mutants has a dramatic effect on the mobility of the α subunit COOH-terminal residues that can be observed directly in electron density images (Figure 7) and quantified with refined temperature factors. The average backbone temperature factors for the α subunits of the 37β mutants, calculated as a percentage change versus βV1M, are plotted in Figure 8. No changes in mobility are observed for the βW37Y mutation (Figure 8e), but the other 37β mutations display significantly increased mobility at the α subunit COOH termini. These are dramatic increases in the mobility of a region that is normally characterized by strong electron density (Figure 7a) and very low temperature factors (Figure 8a). In addition to the increased motility of the backbone atoms of the α subunit COOH termini, the 37β mutations also significantly increase the mobility of the side chains of Tyr140(HC2)α and Arg141(HC3)α (Figure 7). The average side chain temperature factor of Tyr140(HC2)α increases by 82%, 235%, and 129% in the α1 subunits and 171%, 391%, and 255% in the α2 subunits of the βW37A, βW37G, and βW37E mutants, respectively. In contrast, the average side chain temperature factor for Tyr140(HC2)α only increases by 50% and 56% in the α1 and α2 subunits of βW37Y, respectively. The average side chain temperature factors of Arg141(HC3)α increase by 84%, 160%, and 255% in the α1 subunits and by 95%, 259%, and 285% in the α2 subunits of the βW37A, βW37G, and βW37E mutants, respectively. Very little change in the mobility of the Arg141(HC3)α side chain is observed in the βW37Y mutation.

Mutation-Induced Structural Changes in the Switch Region of the α1β2 Interface. The tertiary δ_3 profiles of the βW37A, βW37G, and βW37E mutants also reveal changes in β subunit tertiary structure at the switch region of the α1β2 interface (Figure 3). As shown in Figure 6c, where the β2 subunits have been superimposed, these changes result from mutation-induced changes in the quaternary structure of the α1β2 interface. As the α1β2 interface widens in response to the loss of interactions at the mutation site, residues His97(FG4)β2 through Asn102(G4)β2 shift position so that Asp99(G1)β2, Glu101(G3)β2, and Asn102(G4)β2 maintain intersubunit contacts, respectively, with Asn97(G4)α1, Val96(G3)α1, and Asp94(G1)α1 (via water interactions). In addition (but not shown in Figure 6c), Asp99(G1)β2 maintains van der Waals contact with Thr41(C6)α1 and a hydrogen bond with the side chain of Tyr42(C7)α1. As a consequence, Val98(FG5)β2 is pulled along with these residues as they move toward the α1 subunit and away from the β2 heme. Movement of the β FG corner residues, particularly Val98(FG5)β and Asn102(G4)β, away from the β2 heme results in a small movement of the B pyrrole ring (not shown).

Cross-Validation of Tertiary Structure Changes. The rigid body refinements that were carried out with X-PLOR lowered the R_{free} value for each mutant in crystal form 1 (Table 3), implying that the rigid body movements of the subunits are true improvements to the atomic models. In contrast, the R_{free} values for each mutant increased in an asymptotic manner to higher values during the PROLSQ refinements used to obtain the mutation-induced tertiary structure changes. Taken at face value, the increased R_{free} values suggest that no further improvements in the atomic models were realized as a result of the restrained least-squares PROLSQ refinement. However, the following analysis shows this is not the case.

To address the issue of the increase in R_{free} that follows PROLSQ refinement, an additional set of refinement cycles was carried out on the crystal form 1 structure of βV1M (the surrogate wild-type structure used in this study). The initial refinement of βV1M used all the structure factors with magnitudes greater than 2σ between 8.0 and 2.1 Å resolution (33920 reflections) and resulted in a final R value of 0.176. An R_{free} analysis was not performed during the initial refinement. The data set was now randomly divided into a working set (30 838) and a test set (3082) to be used for R_{free} calculations. As expected, the R and R_{free} values, calculated using the final βV1M atomic model, were both essentially unchanged at 0.177 and 0.172, respectively. However, after 16 additional cycles of PROLSQ refinement (using the same stereochemical target values that were used during the intial refinement) R_{free} increased to 0.223, while R decreased very slightly to a value of 0.173. After a total of 78 cycles (the same number of PROLSQ cycles run in the refinement of βW37Y) R_{free} increased to 0.238, while R decreased to 0.172. The reason for the increase in R_{free} is that the refinement bias (or data "overfitting") has been

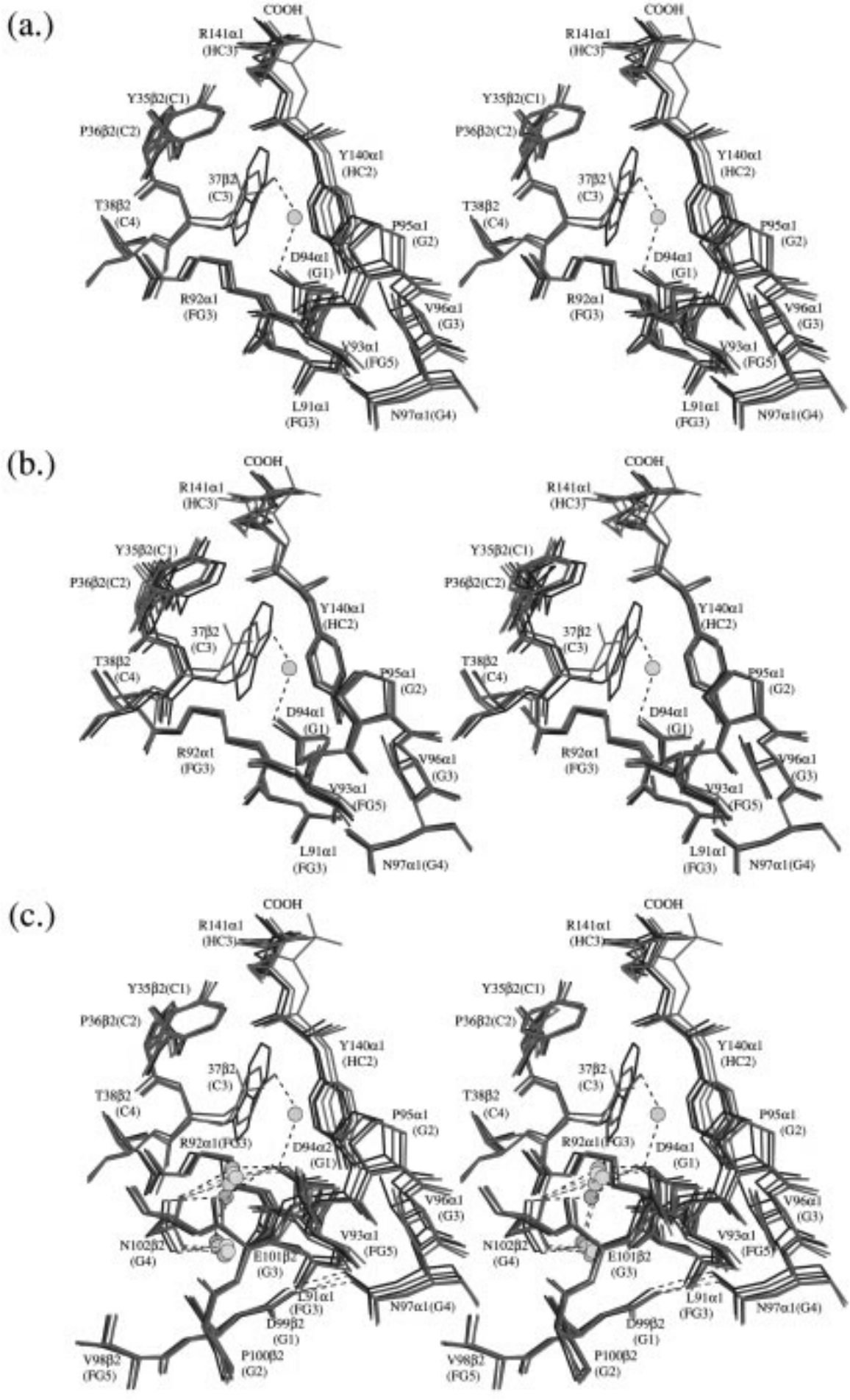
(a.)
COOH
R141α1 (HC3)
Y35β2(C1)
P36β2(C2)
Y140α1 (HC2)
37β2 (C3)
T38β2 (C4)
P95α1 (G2)
D94α1 (G1)
R92α1 (FG3)
V96α1 (G3)
V93α1 (FG5)
L91α1 (FG3)
N97α1(G4)
(b.)
COOH
R141α1 (HC3)
Y35β2(C1)
P36β2(C2)
Y140α1 (HC2)
37β2 (C3)
T38β2 (C4)
P95α1 (G2)
D94α1 (G1)
R92α1 (FG3)
V96α1 (G3)
V93α1 (FG5)
L91α1 (FG3)
N97α1(G4)
(c.)
COOH
R141α1 (HC3)
Y35β2(C1)
P36β2(C2)
Y140α1 (HC2)
37β2 (C3)
T38β2 (C4)
P95α1 (G2)
R92α1(FG3)
D94α2 (G1)
D94α1 (G1)
V96α1 (G3)
N102β2 (G4)
E101β2 (G3)
V93α1 (FG5)
L91α1 (FG3)
N97α1(G4)
D99β2 (G1)
V98β2 (FG5)
P100β2 (G2)

greatly reduced in the test data set by the additional refinement cycles (*42*).

The final R_{free} values for all the crystal form 1 structures (those in Table 3 as well as the βV1M structure) are tightly clustered (varying from 0.238 to 0.259) and well within the range of 0.19−0.33 that Kleywegt and Brünger (*43*) observed for other protein structures at the same resolution. The same is true of the range of *R* values listed in Table 3 (*43*). In the case of βW37Y, the Trp → Tyr mutation results in very small rigid body movements and almost no change in tertiary structure. Thus, while rigid-body refinement reduces R_{free} slightly from 0.214 to 0.199, the tertiary structure refinement of βW37Y is analogous to the additional PROLSQ refinement of the βV1M in that the refinement bias is removed from the test data set and R_{free} increases from an initial value of 0.199 to a final value of 0.256. At the other extreme, the large mutation-induced rigid-body movements in the βW37G produce a "nonisomorphous" crystal structure that has little "memory" of the refinement bias in the βV1M structure. Therefore, rigid-body refinement results in a large decrease in R_{free} from 0.328 to 0.253, and the tertiary structure refinement increases R_{free} only slightly from 0.253 to 0.259. The magnitude of the rigid-body changes in the βW37E structure are almost as large as those in βW37G, and consequently the refinement of the βW37E parallels that of βW37G. On the other hand, because the βW37A mutation produces rigid-body changes in crystal form 1 that are intermediate between those of βW37Y and βW37G, rigid-body refinement results in a moderate drop in R_{free} from 0.249 to 0.212, and tertiary structure refinement results in a moderate increase in R_{free} from 0.212 to 0.244.

Table 3 also contains a refinement summary for βW37Y in crystal form 2 and βW37A in crystal form 3. The crystal form 2 refinement of βW37Y is very similar to that in crystal form 1 except that the decrease in R_{free} following the rigid-body refinement of the tetramer is larger in crystal form 2. Likewise, the tertiary structure refinement of βW37A in crystal form 3 is similar to that in crystal form 1, but in this case there is almost no rigid-body movement in crystal form 3 and consequently there is very little rigid-body associated change in R_{free}.

Since the standard R_{free} parameter is a global statistic, it is not sensitive to local changes in structure (*42*−*44*). In contrast, the R_{free}^{local} parameter is sensitive only to structural changes within the inserted short peptide of the hybrid atomic model (see Materials and Methods). Therefore, genuine mutation-induced changes in tertiary structure should be detectable by a reduction in R_{free}^{local}.

In Figure 9 R_{free}^{local} is plotted versus residue number for the α and β subunits of each mutant structure in crystal form 1 and for the βW37A structure in crystal form 3. In the case of βW37G, obvious minima for R_{free}^{local} are centered at 91α, 101β, and the α COOH terminus (Figure 9a). These minima correspond to δ_3 maxima shown in Figures 2e and 3e, respectively, and the large increase in α COOH-terminal temperature factors shown in Figure 8c. Thus the small mutation-induced changes in α subunit and β subunit tertiary structure that were identified in βW37G by superposition analysis are cross-validated by R_{free}^{local} analysis. As discussed above, the other major features of the βW37G α and β δ_3 plots, those at the α and β NH_2 termini and at α51, probably do not represent true mutation-induced perturbations because they occur only in one subunit, occur in very mobile portions of the hemoglobin tetramer, and/or are absent in the other 37β mutants. These features are not cross-validated by R_{free}^{local} analysis (Figure 9a). The tertiary structure changes associated with βW37E also are cross-validated by corresponding minima in the R_{free}^{local} plots (Figure 9b). In the case of βW37A in crystal form 1, only the structural changes at 101β and the α COOH termini are cross-validated by R_{free}^{local} (Figure 9c). While it is not clear why the mutation-induced changes at α95 are not cross-validated in crystal form 1 of βW37A, they clearly are cross-validated in crystal form 3 (Figure 9e). Lastly, superposition analysis indicated that the mutation-induced changes in βW37Y must be extremely small, and this is consistent with absence of minima in the βW37Y R_{free}^{local} plots in crystal form 1 (Figure 9d) and crystal form 2 (not shown).

Do Mutations at Trp37(C3)β Cause Changes in Fe−*N$^{\epsilon 2}$His(F8) Bond Lengths?* The mutation-induced tertiary structure changes at the FG corners of the α and β subunits and the COOH termini of the α subunits raise the possibility that the Fe−N$^{\epsilon 2}$His(F8) covalent bonds also could be altered. In an effort to detect changes in these bond lengths, stereochemically restrained least-squares refinement cycles were run in which the target value for the Fe−N$^{\epsilon 2}$His(F8) bonds was varied over a narrow range (see Materials and Methods). The residuals between the refined Fe−N$^{\epsilon 2}$His(F8) bond distances and the target values are plotted versus target value in Figure 10a for the α hemes and in Figure 10b for the β hemes. The Fe−N$^{\epsilon 2}$His(F8) bond target values that correspond to residuals of zero are the ones most consistent with the X-ray data. For both the α and β subunits, these "zero residual" Fe−N$^{\epsilon 2}$His(F8) bond lengths are shortened (relative to those of βV1M) by approximately 0.05−0.06 Å in the βW37G and βW37E mutants, whereas the βW37A and βW37Y mutations appear to have little, if any, effect on the Fe−N$^{\epsilon 2}$His(F8) bond lengths.

By themselves these differences in the Fe−N$^{\epsilon 2}$His(F8) bond lengths cannot be considered meaningful because it is not obvious that very small changes in covalent bond lengths can be measured at the resolution of our diffraction data (2.2−2.0 Å). However, the shorter Fe−N$^{\epsilon 2}$His(F8) bond lengths in the βW37G and βW37E mutants correlate well with independent structural and functional studies. Specifically, the βW37G and βW37E mutants (1) have the highest oxygen affinities and are noncooperative (*13*), (2) have the fastest CO combination rates (*14*), and (3) have the highest Fe−N$^{\epsilon 2}$His(F8) resonance Raman stretching frequencies (*15*).

FIGURE 6: Stereo diagrams showing the environment of residue 37β in the α1β2 interfaces of βV1M (black), βW37Y (green), βW37A (dark blue), βW37G (light blue), and βW37E (red). (a) Atomic models have been overlaid following sieve fit superposition of the β2 subunits as in Figure 3. (b) Atomic models have been overlaid following sieve fit superposition of the α1 subunits as in Figure 2. (c) Same stereo diagram as (a) with the addition of residues Val98(FG5)β through Asn102(G4)β. Hydrogen bonds are indicated by dashed lines, and bound water molecules are indicated by filled circles.

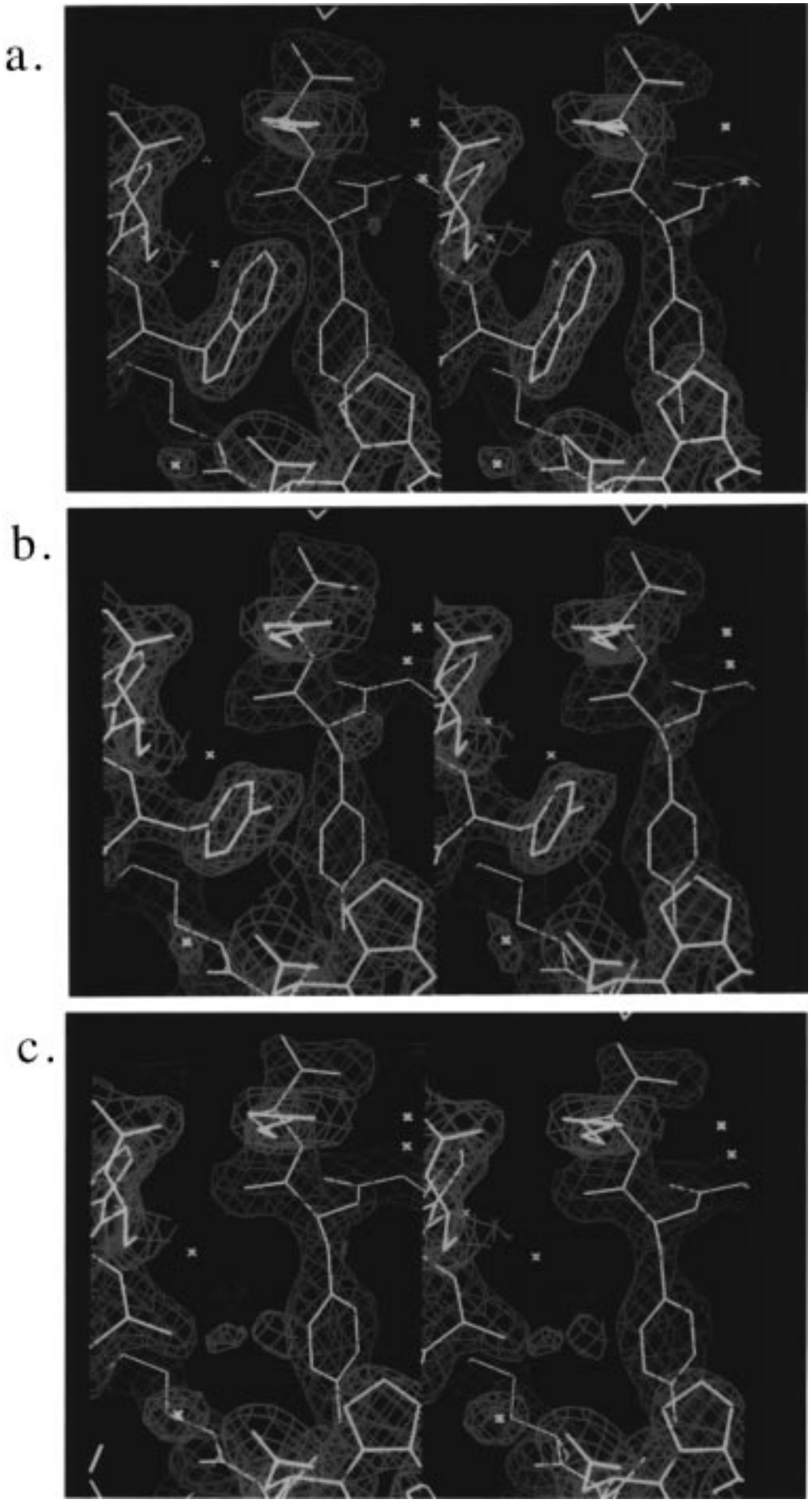
a.
b.
c.

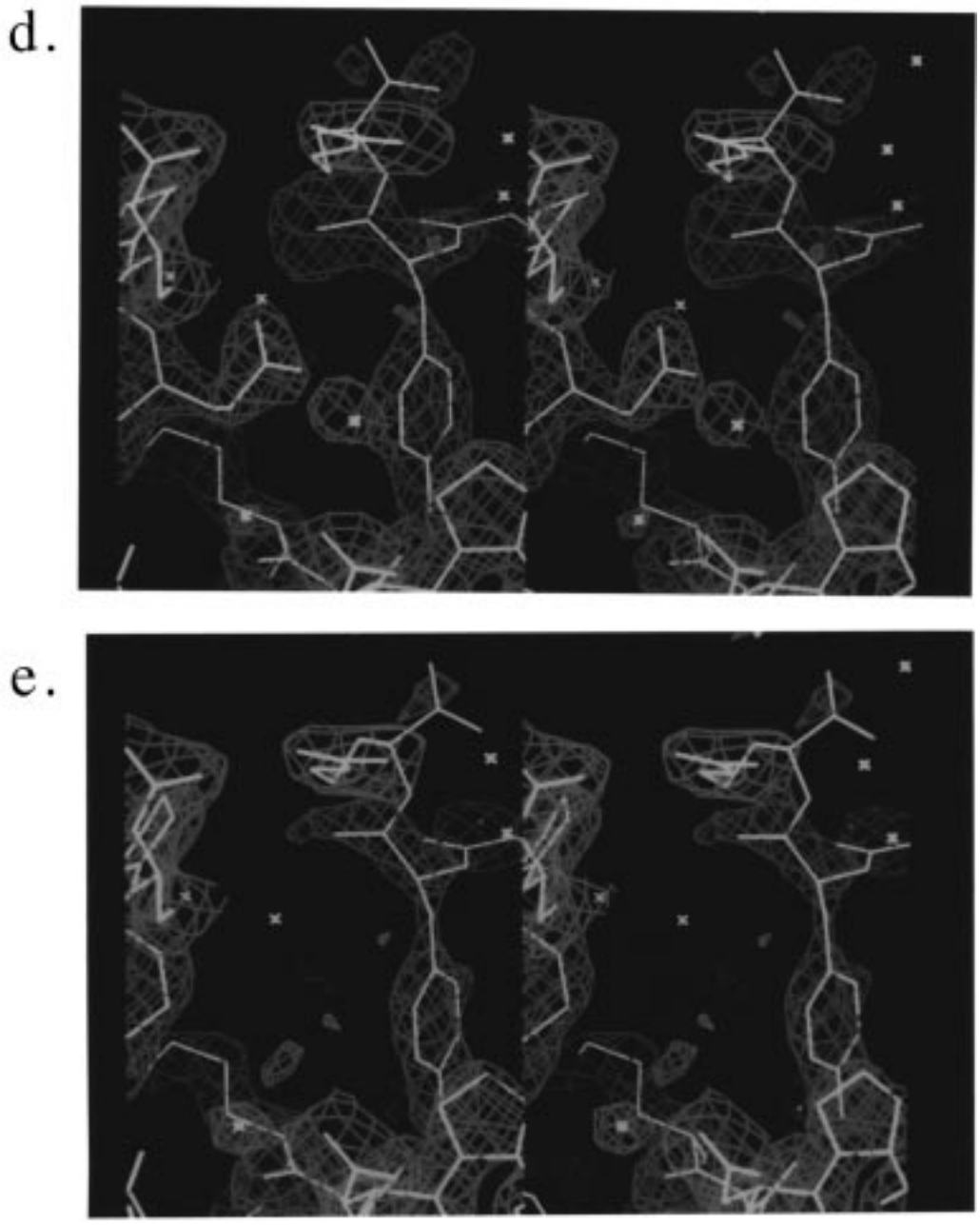

FIGURE 7: Electron density images in the region of residue 37β for the crystal form 1 structures of βV1M (a), βW37Y (b), βW37A (c), βW37E (d), and βW37G (e). The $F_o - F_c$ omit maps are contoured at three times the rms density of the map. Residues Leu86(F7)α through Asn97(G4)α, Leu136(H19)α through the α subunit COOH terminus, and Tyr35(C1)β through Thr38(C4)β were omitted from the atomic models. The atomic models are viewed from the same orientation depicted in Figure 6.

DISCUSSION

When two $\alpha\beta$ dimers associate to form a deoxyhemoglobin $\alpha_2\beta_2$ tetramer, Trp37(C3)β is almost completely buried in the hinge region of the $\alpha1\beta2$ interface where its side chain forms an array of intersubunit contacts. The indole NH group of Trp37(C3)β2 forms a hydrogen bond with the carboxylate side chain of Asp94(G1)α1, and seven of the ten side chain atoms form van der Waals contacts with residues Asp94(G1)α1, Pro95(G2)α1, Tyr140(HC2)α1, and Arg141(HC3)α1. When these interactions and the buried surfaces associated with residue 37β are progressively lost in the βW37Y, βW37A, and βW37G mutants, the structure of the hemoglobin tetramer is progressively disrupted. The structure of the βW37E mutant is disrupted to approximately the same degree as βW37G, but in this case some of the structural changes may be due to the insertion of the large, negatively charged side chain.

The superposition analysis described above has been used to partition these mutation-induced perturbations into quaternary structure changes and tertiary structure changes. Surprisingly, no significant mutation-induced changes in tertiary structure are detected at the mutation site itself for any of the four mutants studied, an observation also reported for the naturally occurring mutant hemoglobin Rothschild, βW37R (*28*). Instead, disruption of the intersubunit contacts associated with Trp37(C3)β results in (1) a change in quaternary structure at the $\alpha1\beta2$ interface, (2) changes in the tertiary structure of the α subunits that are centered at Asp94(G1)α − Pro95(G2)α, (3) changes in the tertiary structure of the β subunits that are located between residues

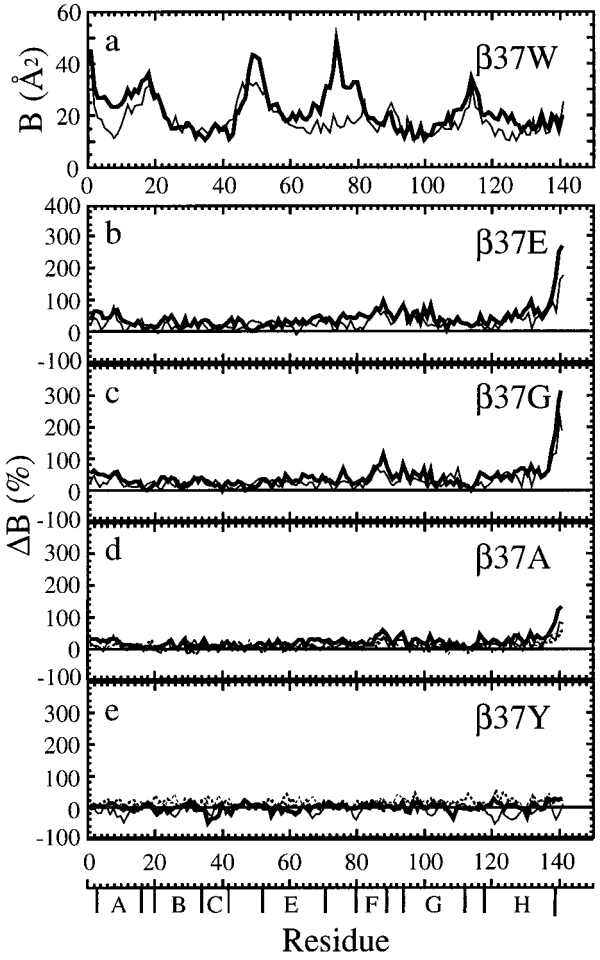

FIGURE 8: Average main chain atom temperature factors for the α1 subunits (thin line) and α2 subunits (thick line) of *β*V1M are plotted versus residue number (a). The percentage change in α subunit main chain temperature factors ($\Delta B = 100(B_{37\beta\ \mathrm{mutant}} - B_{\beta V1M})/B_{\beta V1M}$) is plotted versus residue number for *β*W37E (b), *β*W37G (c), *β*W37A (d), and *β*W37Y (e). In addition, the percentage change in α1 subunit (thin dashed line) and α2 subunit (thick dashed line) main chain temperature factors for *β*W37A in crystal form 3 is plotted in (d) and for *β*W37Y in crystal form 2 in (e).

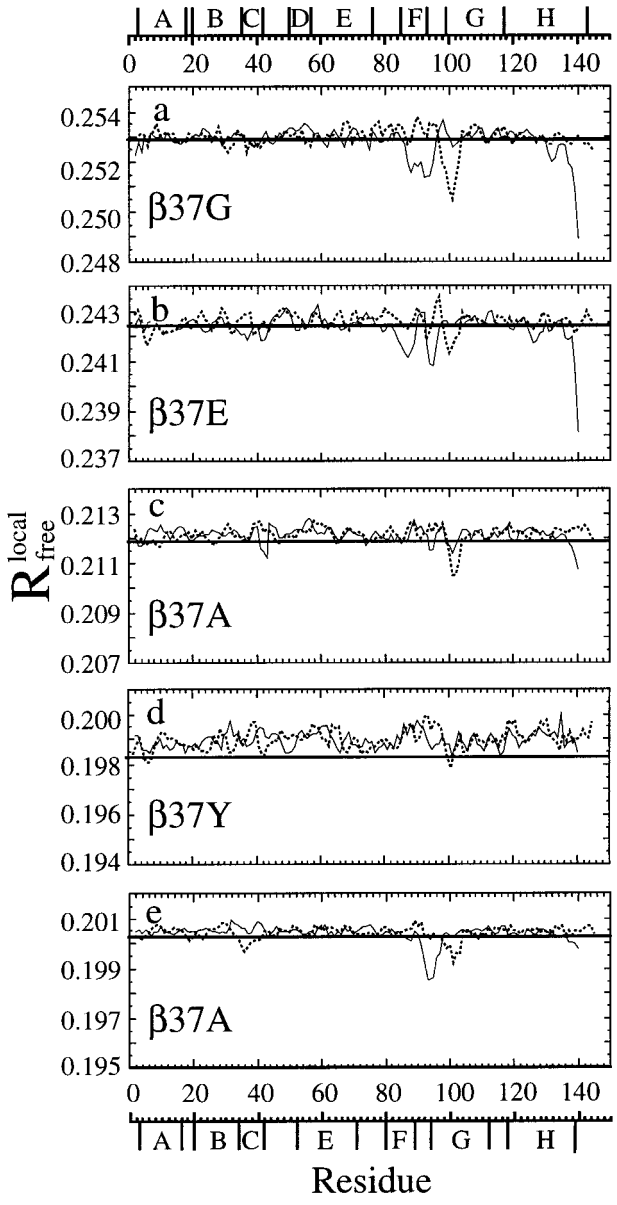

FIGURE 9: R_{free}^{local} parameter plotted versus residue number for the α subunits (thin solid lines) and *β* subunits (dashed lines) of *β*W37G (a), *β*W37E (b), *β*W37A (c), and *β*W37Y (d) in crystal form 1, as well as for the α subunits (thin solid lines) and *β* subunits (dashed lines) of *β*W37A in crystal form 3 (e). The global R_{free} values that were calculated for each 37*β* structure following completion of rigid-body refinement are indicated by the thick horizontal lines. *β* subunit helix boundaries are indicated at the top of the figure, and α subunit helix boundaries are indicated at the bottom.

Asp99(G1)*β* and Asn102(G4)*β*, (4) an increase in the mobility of the α COOH-terminal dipeptide, and (5) a shortening of the Fe−N$^{\epsilon 2}$His(F8) bond in the α and *β* subunits of the *β*W37G and *β*W37E mutants.

The mutation-induced changes in quaternary structure are characterized by rigid body screw rotations that vary in magnitude but not in the direction of the screw rotation axis (Table 4). The rotation angles for the *β*W37Y, *β*W37A, *β*W37E, and *β*W37G mutants are respectively, 0.6°, 1.0°, 1.6°, and 2.0°, respectively. In each case, the translation component of the screw rotation is very small (<0.1 Å), and all the rotation axes pass near the *β* subunit COOH-terminal residue. In this position, the rotation axes are closer to the switch region of the α1*β*2 interface than the hinge region. Therefore, the rigid-body motion results in a significant widening of the α1*β*2 interface at the hinge region (Figure 6a). The change in quaternary structure is smallest for *β*W37Y because intersubunit contacts with Asp94(G1)α and Tyr140(HC2)α are maintained, and the buried surface associated with residue 37*β* does not change much when tryptophan is replaced by tyrosine (157 Å^2 for Trp versus 142 Å^2 for Tyr). Replacing tryptophan with alanine eliminates the direct polar and van der Waals contacts made by the indole group, and this is reflected in a larger opening of the hinge region in the *β*W37A mutant relative to *β*W37Y. The change in quaternary structure is largest for *β*W37G because all of the stabilizing factors associated with the tryptophan side chain are lost in this mutant, including the buried surface area associated with the α-methylene group. Almost all the strong intersubunit contacts associated with Trp37(C3)*β* also are lost in the *β*W37E mutant, but in this case 110 Å^2 of side chain surface area are buried, so that the quaternary structure perturbation is not as great as in the *β*W37G mutant.

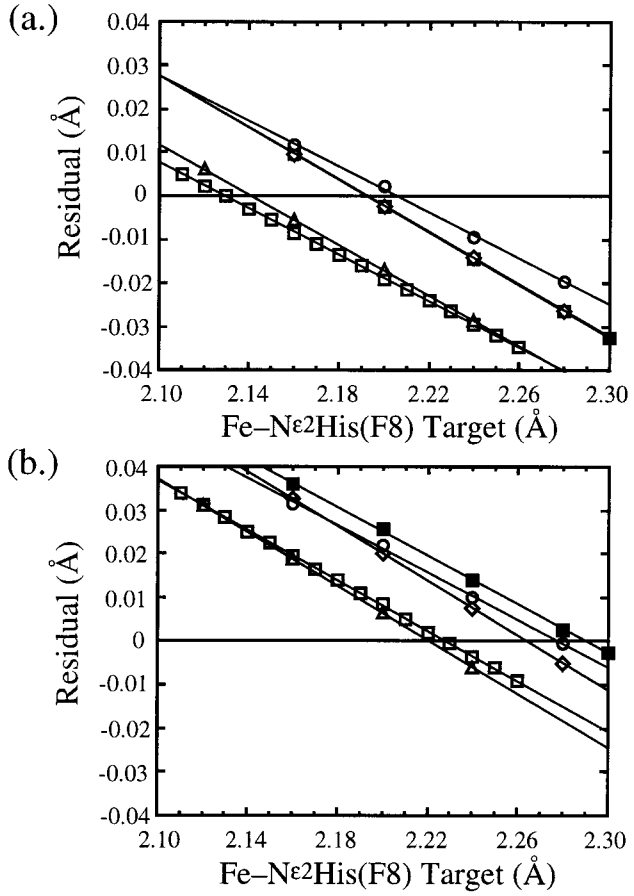

FIGURE 10: Residuals between the refined heme Fe−N$^{\epsilon 2}$His(F8) bond length and its target value are plotted versus the target value for the α subunit hemes (a) and for the β subunit hemes (b) of βV1M (■), βW37Y (◇), βW37A (○), βW37G (△), and βW37E (□).

The changes in α subunit tertiary structure appear to result from the loss of intersubunit contacts between Trp37(C3)β2 and α1 subunit residues Asp94(G1)α1 and Pro95(G2)α1. In particular, in βV1M the carboxyl group of the Asp94(G1)α1 forms a "polar bridge" across the α1β2 interface by making hydrogen bonds with both the backbone NH group of Val96(G3)α1 and the indole NH of Trp37(C3)β2. In the βW37A, βW37E, and βW37G mutants where these interactions are lost completely, the backbone atoms of residues Asp94(G1)α1 and Pro95(G2)α1 move (as measured by δ_1 values) 0.22−0.42 Å away from Trp37(C3)β2 and the α1β2 interface. The same residues, however, have δ_1 shifts of only 0.17−0.22 Å in the βW37Y mutant where Tyr37(C3)β2 continues to interact with Asp94(G1)α1 (see Figure 6b). In the βW37Y mutant, the hydrogen bond with the indole NH is replaced with an interaction with the tyrosine OH group via a water molecule. In addition, a carboxyl oxygen of Asp94(G1)α1 is close (∼3.5 Å) to the C$^{\epsilon 1}$ atom of Tyr37(C3)β2, forming an aromatic C−H···O hydrogen bond of the type described by Derewenda et al. (1995). Thus in wild-type hemoglobin, and to a lesser extent in βW37Y, formation of the polar bridge distorts the backbone of Asp94(G1)α1 and adjacent α1 residues by pulling them into the α1β2 interface. Elimination of the polar bridge [as well as van der Waals contacts with Pro95(G2)α1] in βW37A, βW37E, and βW37G allows this segment of the α1 subunit to relax to a position that may exist in free αβ dimers. Similar shifts of residues Asp94(G1)α and Pro95(G2)α were first observed in deoxyhemoglobin Rothschild (βW37R), and it was asserted that "the disruption of the Trp → Arg mutation pushes these residues away from the α1β2 interface" (*28*). However, in light of the findings for the recombinant 37β mutants, the shifts observed in deoxyhemoglobin Rothschild are most likely the result of the relaxation of steric constraints rather than the creation of steric repulsion.

The mutation-induced changes in the quaternary structure of the α1β2 interface and the tertiary structure of the α hinge residues Leu91(FG3)α1−Val96(G3)α1 are directly linked

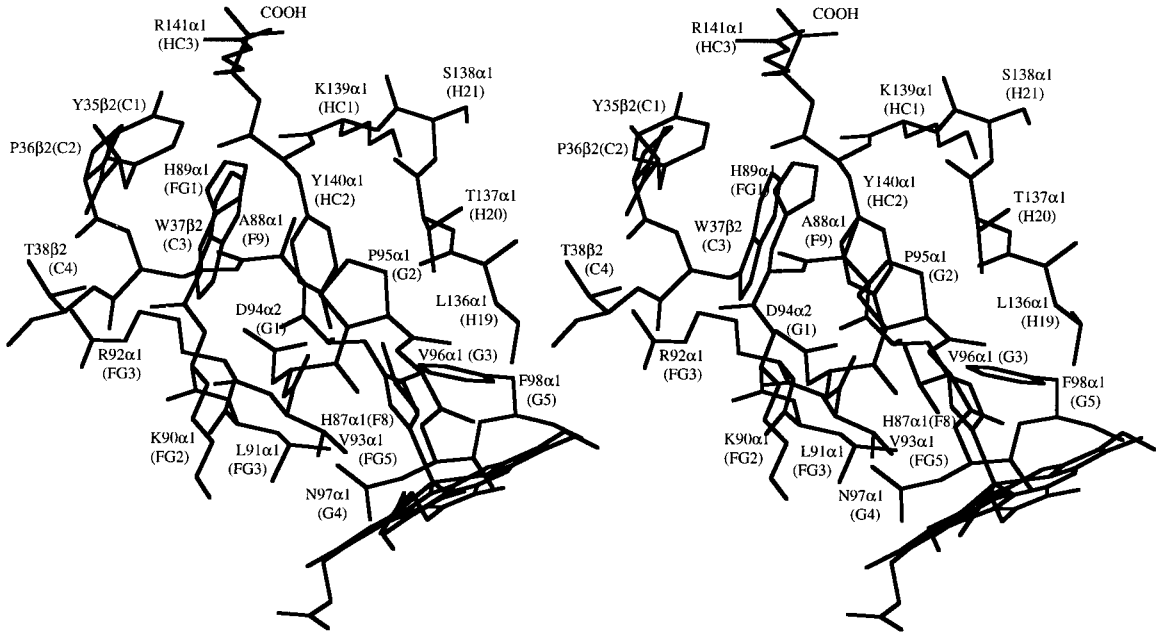

FIGURE 11: Stereo diagram of the Tyr140(HC2)α1 pocket in deoxyhemoglobin βV1M. The view is the same as that in Figure 6a, with the addition of α1 subunit residues His87(F8)α through Lys90(FG2)α and Leu136(H19)α through Lys139(HC1)α. The side chain of Tyr140(HC2)α is buried between the α1β2 interface and the end of the α1 F helix. In particular, the side chain is located directly between the side chain of Trp37(C3)β2 and the proximal histidine His87(F8)α and residue Ala88(F9)α. In this position the side chain of Tyr140(HC2)α1 makes direct contacts with the proximal histidine and the α1β2 interface.

to the tertiary structure changes of the β switch residues Leu96(FG3)β2−Asn102(G4)β2. As the $\alpha1\beta2$ interface opens, these residues of the β FG corner and β G helix shift position in order to maintain close contacts with residues of the α FG corner/G helix (see Figure 6c). Thus this linkage between the hinge and switch regions of the T quaternary structure provides a pathway by which structural changes on one side of the $\alpha1\beta2$ interface are communicated to the other side. Moreover, because residues α FG3 and α FG5 are in direct contact with the α heme, and residues β FG3, β FG5, and β G4 are in direct contact with the β heme, the mutation-induced structural changes extend to both the α and β heme groups. Ligation-induced changes in structure may propagate between subunits along the same pathway in the T-structure.

In the T-structure, Tyr140(HC2)α1 forms intersubunit contacts of less than 4.0 Å with Trp37(C3)β2 and Pro36(C2)β2, as well as intrasubunit contacts of less than 4.0 Å with His87(F8)α1, Ala88(F9)α1, Arg92(FG4)α1, Val93(FG5)α1, Pro95(G2)α1, Phe98(G5)α1, Leu136(H19)α1, Thr137(H20)α1, and Ser138(H21)α1 (see Figure 11). These residues form a tight pocket that constrains the side chain of Tyr140(HC2)α and reduces its mobility; the average temperature factor for the side chain atoms is 10 Å^2. According to the stereochemical mechanism of Perutz (*2*), oxygen binding to the α heme in the T-structure results in expulsion of Tyr140(HC2)α from its pocket. The constraints present in wild-type deoxyhemoglobin resist the movement of Tyr140(HC2)α from its pocket, creating ligand-induced tension and the low oxygen affinity characteristic of the wild-type tetramer. In the βW37A, βW37E, and βW37G mutants, the interactions between Tyr140(HC2)α1 and Trp37(C3)β2 are lost as a direct result of the mutation, and the interactions with the other pocket residues are weakened as a result of the mutation-induced changes in quaternary structure and subunit tertiary structure discussed above. As a result, the temperature factors for the backbone atoms of the α COOH-terminal dipeptide increase dramatically (Figure 8), and the average side chain atomic temperature factor of Tyr140(HC2)α increases to 22, 28, and 39 Å^2 for βW37A, βW37E, and βW37G, respectively. The progressive increase in the mobility of the α subunit COOH-terminal dipeptide corresponds to progressively weaker electron density images for these residues (Figure 7). Because of this increased mobility, critical salt bridges formed by Arg141(HC3)α (*2*) are gradually weakened, Tyr140(HC2)α is more easily expelled from its pocket, and ligand-induce tension is greatly reduced. Thus these mutants have increased oxygen affinity, reduced cooperativity, and increased CO combination rates (*13*, *14*). In the case of βW37Y, direct contacts between Tyr140(HC2)α1 and Tyr37(C3)β2 are maintained, the interactions with the other pocket residues are weakened to a much more limited degree, and the average side chain atomic temperature factors of Tyr140(HC2)α increase to only 15 Å^2. Therefore, βW37Y is structurally and functionally much more similar to wild-type deoxyhemoglobin.

In addition to ligand-induced tension, the low affinity of deoxyhemoglobin also may be due in part to preexisting tension in the T-structure. Kitagawa (*46*) correlated the Fe−N$^{\epsilon2}$His(F8) bond stretching frequency (ν_{Fe-His}) with the first Adair constant for deoxyhemoglobin A as well as with several variant deoxyhemoglobins. He concluded that the Fe−N$^{\epsilon2}$His(F8) bond is stretched in the T-structure and that the "strain on the Fe−N$^{\epsilon2}$His(F8) bond imposed by the globin is evidently one of the important factors that control oxygen affinity". Peterson et al. (*15*) report in the accompanying paper that ν_{Fe-His} increases in the order deoxyhemoglobin A < βW37Y < βW37A < βW37E < βW37G, indicating that the strain on the Fe−N$^{\epsilon2}$His(F8) bond is progressively reduced in these mutants. Consistent with these observations, we find that the length of the Fe−N$^{\epsilon2}$His(F8) bond is decreased, relative to deoxyhemoglobin A, in the deoxy structures of βW37E and βW37G, the 37β mutants that are the most perturbed structurally and functionally. This suggests that relaxing constraints on Tyr140(HC2)α allows the Fe−N$^{\epsilon2}$His(F8) bond to relax in the deoxy T-structure.

REFERENCES

1. Mills, F. C., Johnson, M. L., and Ackers, G. K. (1976) *Biochemistry 15*, 5350−5362.
2. Perutz, M. F. (1970) *Nature 228*, 726−734.
3. Baldwin, J. M., and Chothia, C. (1979) *J. Mol. Biol. 129*, 175−220.
4. Perutz, M. F. (1989) *Q. Rev. Biophys. 22*, 139−236.
5. Turner, G. J., Galacteros, F., Doyle, M. L., Hedlund, B., Pettigrew, D. W., Turner, B. W., Smith, F. R., Moo-Penn, W., Rucknagel, D. L., and Ackers, G. K. (1992) *Proteins 14*, 333−350.
6. Kavanaugh, J. S., Chafin, D. R., Arnone, A., Mozzarelli, A., Rivetti, C., Rossi, G. L., Kwiatkowski, L. D., and Noble, R. W. (1995) *J. Mol. Biol. 248*, 136−150.
7. Sasaki, J., Imamura, T., and Yanase, T. (1978) *J. Biol. Chem. 253*, 87−94.
8. Sharma, V. S., Newton, G. L., Ranney, H. M., Ahmed, F., Harris, J. W., and Danish, E. H. (1980) *J. Mol. Biol. 144*, 267−280.
9. Ishimori, K., Imai, K., Miyazaki, G., Kitagawa, T., Wada, Y., Morimoto, H., and Morishima, I. (1992) *Biochemistry 31*, 3256−3264.
10. Owen, M. C., Ockelford, P. A., and Wells, R. M. (1993) *Hemoglobin 17*, 513−521.
11. Britain, T. (1994) *Biochem. J. 300*, 553−556.
12. Vallone, B., Bellelli, A., Miele, A. E., Brunori, M., and Fermi, G. (1996) *J. Biol. Chem. 271*, 12472−12480.
13. Kiger, L., Klinger, A. L., Kwiatkowski, L. D., De Young, A., Doyle, M. L., Holt, J. M., Noble, R. W., and Ackers, G. K. (1999) *Biochemistry 37*, 4336−4345.
14. Kwiatkowski, L. D., Hui, H. L., Wierzba, A., Noble, R. W., Walder, R. Y., Peterson, E. S., Sligar, S. G., and Sanders, K. E. (1998) *Biochemistry 37*, 4325−4335.
15. Peterson, E. S., and Friedman, J. M. (1998) *Biochemistry 37*, 4346−4357.
16. Hernan, R. A., Hui, H. L, Andracki, M. E., Noble, R. W., Sligar, S. G., Walder, J. A., and Walder, R. Y. (1992) *Biochemistry 31*, 8619−8628.
17. Doyle, M. L., Lew, G., De Young, A., Kwiatkowski, L., Wierzba, A., Noble, R. W., and Ackers, G. K. (1992) *Biochemistry 31*, 8629−8639.
18. Kavanaugh, J. S., Rogers, P. H., and Arnone, A. (1992) *Biochemistry 31*, 8640−8647.
19. Riggs, A. (1981) *Methods Enzymol. 76*, 5−29.
20. Ward, K. B., Wishner, B. C., Lattman, E. E., and Love, W. E. (1975) *J. Mol. Biol. 98*, 161−177.
21. Arnone, A., Rogers, P. H., and Briley, P. D. (1980) in *Biophysics and Physiology of Carbon Dioxide* (Bauer, C., Gros, G., and Bartels, H., Eds.) pp 67−74, Springer-Verlag, Berlin.
22. Metzler, C. M., Rogers, P. H., Arnone, A., Martin, D. S., and Metzler, D. E. (1979) *Methods Enzymol. 62*, 551−558.
23. Greer, J. (1971) *J. Mol. Biol. 59*, 107−126.
24. Fitzgerald, P. M. D., and Love, W. E. (1979) *J. Mol. Biol. 132*, 603−619.
25. Perutz, M. F. (1968) *J. Crystal Growth 2*, 54−56.

26. Howard, A. J., Nielson, C., and Xuong, N. H. (1985) *Methods Enzymol. 114*, 452−472.
27. Brünger, A. T. (1992) *Nature 355*, 472−474.
28. Kavanaugh, J. S., Rogers, P. H., Case, D. A., and Arnone, A. (1992) *Biochemistry 31*, 4111−4121.
29. Hendrickson, W. A. (1985) *Methods Enzymol. 115*, 252−270.
30. Sheriff, S. (1987) *J. Appl. Crystallogr. 20*, 53−55.
31. Cambillau, C. (1989) in *Silicon Graphics Geometry Partners Directory*, spring vol. p 61, Silicon Graphics, Mountain View, CA.
32. Jones, T. A. (1985) *Methods Enzymol. 115*, 157−189.
33. Brünger, A. T. (1992) *XPLOR, Version 3.1*, Yale University Press, New Haven and London.
34. Laskowski, R. A., MacArthur, M. W., Moss, D. S., and Thornton, J. M. (1993) *J. Appl. Crystallogr. 26*, 283−291.
35. Harutyunyan, E. H., Safonova, T. N., Kuranova, I. P., Popov, A. N., Teplyakov, A. V., Obmolova, G. V., Rusakov, A. A., Vainshtein, B. K., Dodson, G. G., Wilson, J. C., and Perutz, M. F. (1995) *J. Mol. Biol. 251*, 104−115.
36. Kabsch, W. (1976) *Acta Crytstallogr., Sect. A 32*, 922−923.
37. Yuen, P. S., and Nyburg, S. C. (1979) *J. Appl. Crystallogr. 12*, 258.
38. Gerstein, M., and Chothia, C. (1991) *J. Mol. Biol. 220*, 133−149.
39. Cox, J. M. (1967) *J. Mol. Biol. 28*, 151−156.
40. Lee, B., and Richards F. M. (1971) *J. Mol. Biol. 55*, 379−400.
41. Matthews, B. W. (1968) *J. Mol. Biol. 33*, 491−497.
42. Brünger, A. T. (1993) *Acta Crystallogr. D49*, 24−36.
43. Kleywegt, G. J., and Brünger, A. T. (1996) *Structure 4*, 897−904.
44. Kleywegt, G. J., and Jones T. A. (1995) *Structure 3*, 535−540.
45. Derewenda, Z. S., Lee, L., and Derewenda, U. (1995) *J. Mol. Biol. 252*, 248−262.
46. Kitagawa, T. (1992) *Prog. Biophys. Mol. Biol. 58*, 1−18.

BI9708702